

This is the peer reviewed version of the following article:

Jovanović B, Caspee R, Reynders E, Lombaert G, Put F, Lucherini A, et al.
Experimental investigation on the effect of natural fire exposure on the post-fire behavior of reinforced concrete beams using electric radiant panel. *Structural Concrete*. 2025;26(3):3629–44.

which has been published in final form at <https://doi.org/10.1002/suco.202400550>.
This article may be used for non-commercial purposes in accordance with Wiley Terms and Conditions for Use of Self-Archived Versions. This article may not be enhanced, enriched or otherwise transformed into a derivative work, without express permission from Wiley or by statutory rights under applicable legislation. Copyright notices must not be removed, obscured or modified. The article must be linked to Wiley's version of record on Wiley Online Library and any embedding, framing or otherwise making available the article or pages thereof by third parties from platforms, services and websites other than Wiley Online Library must be prohibited.

1 Experimental investigation on the effect of
2 natural fire exposure on the post-fire
3 behaviour of reinforced concrete beams
4 using electric radiant panel

5 Balša Jovanović¹, Robby Caspeele², Edwin Reynders³, Geert Lombaert⁴, Florian Put⁵, Andrea Lucherini⁶,
6 Ruben Van Coile⁷

7 **Abstract**

8 In this study, the effects of natural fire exposure on the post-fire behaviour of concrete beams are
9 investigated. The study is based on laboratory tests where three reinforced concrete beams were

¹Corresponding author

PhD student, Department of Structural Engineering and Building Materials, Ghent University, Belgium

Department of Civil Engineering, Structural Mechanics Section, KU Leuven, Belgium,

e-mail: Balsa.Jovanovic@ugent.be, ORCID: <https://orcid.org/0000-0001-5200-5848>

²**Professor, Department of Structural Engineering and Building Materials, Ghent University, Belgium,**

e-mail: Robby.Caspeele@ugent.be, ORCID: <https://orcid.org/0000-0003-4074-7478>

³**Professor, Department of Civil Engineering, Structural Mechanics Section, KU Leuven, Belgium,**

e-mail: Edwin.Reynders@kuleuven.be, ORCID: <https://orcid.org/0000-0002-1042-0282>

⁴**Professor, Department of Civil Engineering, Structural Mechanics Section, KU Leuven, Belgium,**

e-mail: Geert.Lombaert@kuleuven.be, ORCID: <https://orcid.org/0000-0002-9273-3038>

⁵**PhD student, Department of Structural Engineering and Building Materials, Ghent University, Belgium**

e-mail: Florian.Put@UGent.be, ORCID: <https://orcid.org/0000-0002-4522-9015>

⁶**PhD, Senior Researcher, Slovenian National Building and Civil Engineering Institute (ZAG), Slovenia**

e-mail: Andrea.Lucherini@zag.si, ORCID: <https://orcid.org/0000-0001-8738-1018>

⁷**Professor, Department of Structural Engineering and Building Materials, Ghent University, Belgium,**

e-mail: Ruben.VanCoile@ugent.be, ORCID: <https://orcid.org/0000-0002-9715-6786>

10 subjected to fire exposure using an electric radiant panel. This panel enables a precise application of
11 radiative heat exposure closely mimicking natural fire exposure in a safe manner. During the test, the
12 deflections, deformations and temperature changes are measured for all three concrete beams.
13 Additionally, Finite Element Modeling (FEM) is applied to supplement these tests, demonstrating the
14 performance of existing structural fire engineering calculation tools in evaluating the burnout
15 performance of concrete beams.

16 The results of the tests show that the electric radiant panel provide a novel approach for fire simulation
17 which is effective in replicating natural fire conditions, by applying the heat flux as specified in the
18 Eurocode Parametric Fire Curve in a highly controlled manner. The uniformity of the temperature field
19 measured inside the beams and the consistent deformations observed during the heat exposure across
20 all three tests underscores the accuracy of the fire simulation. Furthermore, post-fire assessments
21 reveal that while the exposed beams suffered some reduction in load-bearing capacity, they retained
22 a significant portion of their original strength that was consistent across all three beams.

23 The numerical simulations conducted in this study demonstrate a high level of accuracy in predicting
24 the behaviour of the concrete beams during fire exposure. These simulations effectively mirrored the
25 experimental results, validating that they are a valuable tool for assessing concrete structures'
26 performance in fire scenarios.

27 1. Introduction

28 Due to their thermal and mechanical properties, concrete members are highly resistant to fire exposure
29 and in a large number of cases survive fire exposure without collapsing [1], [2]. Understanding the
30 behaviour of concrete structures after fire exposure is essential for several reasons. First and foremost,
31 post-fire assessment provides valuable insights into the extent of damage incurred during a fire.
32 Additionally, it enables engineers and researchers to evaluate the residual load-carrying capacity of
33 such structures in the aftermath of a fire event. This knowledge is crucial for determining whether a
34 structure remains safe for occupancy or requires immediate repair or rehabilitation. This information

35 is key in guiding structural repair and retrofitting efforts, ultimately contributing to the overall safety
36 and longevity of concrete buildings and infrastructure [3].

37 Fires not only subject structures to elevated temperatures but also induce complex thermal and
38 mechanical interactions within the materials. These interactions can lead to changes in material
39 properties, microcracking, and even structural deformations, all of which have direct implications on
40 the safety and performance of concrete structures [4].

41 In order to accurately predict and understand the post-fire behaviour of concrete members, their
42 behaviour during the fire must also be known and understood. One approach to achieve this is through
43 experimental testing, where structural members are tested at full scale while being exposed to the
44 entire fire progression, including both the heating and cooling phases. In order to properly understand
45 the residual behaviour for research purposes, structural members can be tested at full scale while
46 exposed to the whole progression of the fire including both the heating and the cooling phase. While
47 large-scale tests provide valuable insights into fire-induced damage, they often come with significant
48 financial and logistical efforts. Additionally, due to the difficulty of controlling the exact fire exposure,
49 the repeatability of these tests can be difficult to achieve. Moreover, accurately following prescribed
50 cooling phases in these tests can be inherently challenging, potentially limiting their practicality. The
51 importance of the cooling phase and the difficulties in employing it in large-scale tests have been
52 demonstrated in [5].

53 For those reasons, there has been an emerging trend of developing methods to directly control the
54 thermal boundary conditions to the test specimens. One example is the H-TRIS system [6] which
55 employs a gas-powered radiant panel that can precisely control the applied heat flux to the sample by
56 adjusting the distance between the panel and the sample. In the work presented here, a similar
57 technique employing an electric intensity-controlled radiant panel is used.

58 An experimental program was developed which focuses on the assessment of the behaviour of
59 concrete beams after exposure to fire. The experiments aim to replicate fire exposure through

60 controlled heating and loading conditions. Four identical concrete beams are considered, including one
61 beam serving as a reference which is not exposed to the fire. These tests are designed to evaluate the
62 beams' structural response, including deflections, deformations, and temperature distributions, during
63 and after the simulated fire exposure. The comprehensive instrumentation system employed in this
64 study includes load cells, LVDTs, thermocouples, and Digital Image Correlation (DIC), enabling precise
65 data collection and analysis. In addition to the experimental program, finite element modelling (FEM)
66 is used to simulate the structural response of concrete beams. This added dimension demonstrates the
67 ability of current modelling approaches, particularly in simulating fires with cooling phases. The
68 inclusion of FEM provides a more nuanced examination of structural responses during the fire
69 exposure, complementing the insights gained from the experimental phase. In the following, the
70 experimental program and results are presented in sections 2 and 3. Section 4 elaborates on the
71 numerical modelling

72 2. Experimental program

73 Four identical concrete beams are tested (B1, B2, B3 and BR). Beams B1, B2 and B3 are exposed to the
74 heating regime simulating natural fire exposure and beam BR is kept as a reference and is not exposed
75 to the heating. The testing consists of three stages. The first stage is the mechanical loading and
76 unloading until the “serviceability” load (in this case 67% of the beams’ design bending capacity). This
77 stage is conducted to make a distinction between cracks induced by regular damage and additional
78 accidental fire damage. These tests are conducted to assess the damage level of the beams prior to the
79 fire exposure. This is done to allow for a subsequent comparison with the damage level assessed post-
80 fire. All four beams are subjected to this first loading stage. The second stage is the heating stage where
81 thermal loading is imposed using an electrical radiant panel, while the mechanical load is kept constant.
82 Finally, the third stage is conducted to determine the residual bending capacity of all four beams
83 through a four-point flexural bending test.

84 2.1. Beam description

85 All four beams utilized in the experimental campaign are identical in terms of their dimensions and are
86 cast from the same batch of concrete. The constituents of the concrete mix are listed in Table 1. These
87 beams have a length of 3.8 meters, a cross-sectional height of 0.29 m, and a width of 0.2 m. Each beam
88 is reinforced with a total of 5 steel rebars, each having a diameter of 16 mm. Among these rebars, 3
89 are positioned in the tensioned zone of the beam, while the remaining 2 are placed in the compressed
90 zone. A concrete cover of 20 mm (from all edges) is maintained for all 5 bars. The selection of this
91 relatively low cover thickness compared to the usual design was deliberate, aiming at the investigation
92 of concrete beams that are more susceptible to fire exposure. To enhance the structural integrity, 8
93 mm stirrups are employed as shear reinforcement, spaced at 20 cm intervals along the length of the
94 beams. The tested beams are made of C30/37 concrete with siliceous aggregate and B500B steel is
95 used for the reinforcement. The design moment capacity is equal to 61.6 kNm according to the
96 calculation approach presented in [7].

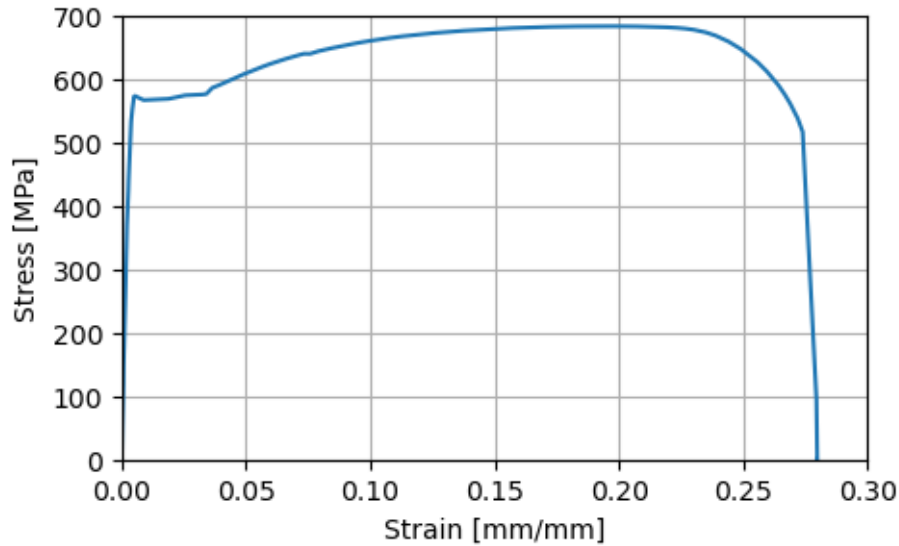
97 *Table 1 Concrete mix constituents*

Materials	Weight [kg/m ³]	Mixing ratios [-]
Cement	330	1.00
Coarse aggregate (4/20)	995	3.02
River sand (0/2)	453	1.37
Crushed sand (0/4)	371	1.12
Water	189	0.55

98

99 The mechanical properties of the concrete are assessed after 28 days on 3 standard cubes (150 mm x
100 150 mm x 150 mm) and 3 standard cylinders (diameter 150 mm, height 300 mm). The samples were
101 stored at the same ambient conditions as the beams themselves. The compressive strength results for
102 the cubes is $f_{c,cube} = 45.7 \text{ MPa}$ with a standard deviation of 2.0 MPa, for the cylinders the strength is

103 $f_c = 38.8 \text{ MPa}$ and a standard deviation of 1.8 MPa. Furthermore, the tensile reinforcement was also
104 tested. The measured yield strength is $f_y = 565 \text{ MPa}$, ultimate strength $f_u = 683 \text{ MPa}$ and modulus
105 of elasticity $E_s = 213 \text{ GPa}$. The stress strain diagram is presented in Figure 1

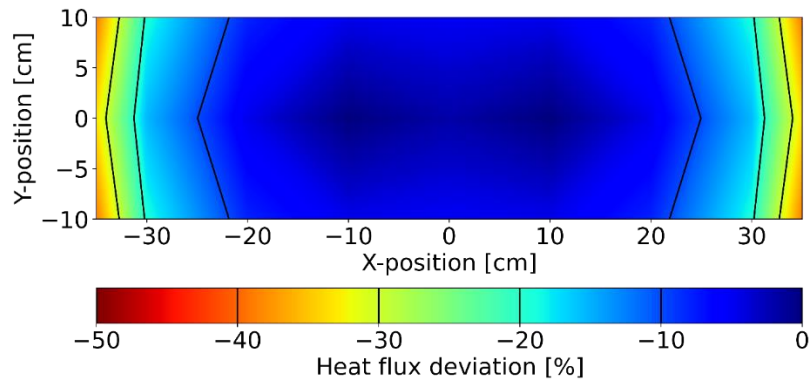


106

107 *Figure 1. Measured stress-strain diagram for the reinforcement bars*

108 2.2. Panel description

109 In order to replicate fire exposure conditions for experimental purposes, a innovative high-intensity
110 electric radiant panel is employed. This panel has been custom developed and comprises 21 individual
111 emitters, each measuring 500 mm in length, emitting short-wavelength infrared radiation at high-
112 intensity levels. These emitters collectively cover an area of approximately 900 mm x 500 mm. The
113 emitters are protected by a removable quartz glass panel. When operating at its maximum intensity,
114 the panel can generate an approximately uniform radiative heat flux of 100 kW/m^2 over an area
115 measuring 200 mm x 700 mm, positioned at a distance of 100 mm from its protective glass. The
116 measured distribution of the radiative heat flux deviation compared to the central position over that
117 area is shown in Figure 2. The measurements are conducted using a Schmidt-Boelter heat flux gauge
118 positioned at different positions in a grid with with spacing of 10 cm.



119

120 *Figure 2 Radiant panel heat flux deviation compared to the central position over the exposed beam area at a 100 mm distance*
 121 *from the panel.*

122 Precise control over the radiation intensity of the panel is achievable through voltage manipulation as
 123 an input signal. This control mechanism facilitates the control of the radiative heat flux to which the
 124 specimen is exposed based on the previously obtained calibration of the voltage-heat flux relationship
 125 [8]. Consequently, it becomes possible to simulate the total heat flux that the specimen would
 126 encounter during a fire event at any given point in time, including the decay and cooling phases [9].
 127 This control process is executed using a Python-based in-house program hosted on a PC which allows
 128 for dynamic adjustment and monitoring of the radiant heat flux. Further information on the panel
 129 characteristics is described in [8].

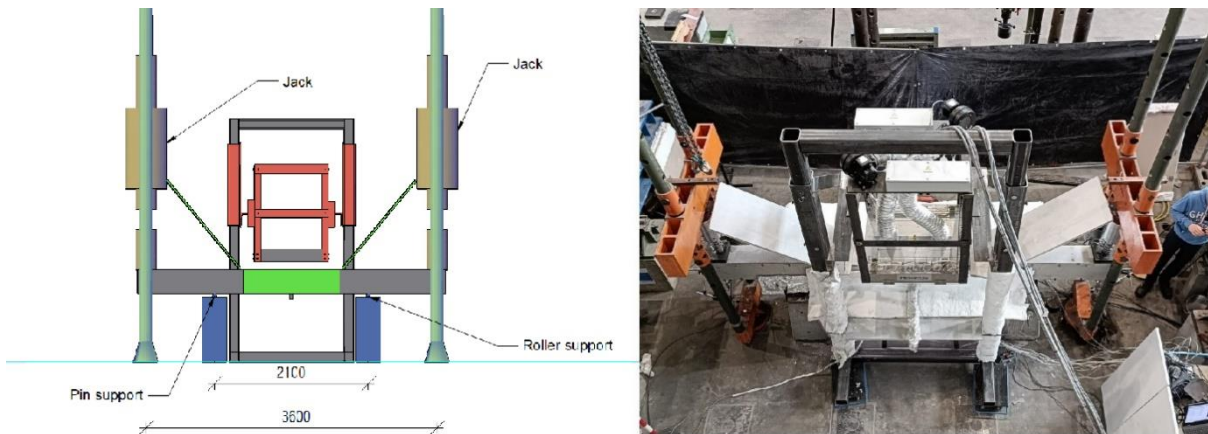
130 In the case of a real fire, more precisely a structurally significant flashover compartment fire, the heat
 131 is mainly transferred to the structure through convection and radiation [9]. Similarly, the heat transfer
 132 to structural elements in accordance with the Eurocode is determined considering convection and
 133 radiation relative to a specified temperature-time curve. However, the electric radiant panel is only
 134 able to provide radiative heat transfer to the beam specimen. In order to approximate the heat transfer
 135 scenario with both convection and radiation, first the total heat flux incoming to the specimen from
 136 the chosen temperature-time curve is calculated. This is done numerically using a 1-dimensional finite
 137 difference heat transfer model. The surface temperature is calculated based on the convective and
 138 radiative heat transfer from the specified temperature-time curve. Finally, using the obtained surface
 139 temperature the radiative heat flux needed from the radiation panel to obtain the same total heat flux

140 on the surface is calculated. It is obtained under the assumption that the convective heat transfer on
141 the exposed surface is negligible. This assumption is derived based on the preliminary tests where it
142 was evident that, due to the small distance between the panel and the exposed beam surface (100
143 mm), the air in the gap is at temperatures similar to the temperature of the surface and the heated
144 protective glass of the panel. This assumption is further confirmed by comparing the simulated and
145 measured temperatures inside the beams during the tests.

146 2.3. Setup description

147 During the first stage of the experiment, the mechanical loading was applied in a reversed four-point
148 bending setup (Figure 3). For safety considerations, the setup was reversed from its standard
149 configuration (upside down) in the first two stages. Specifically, the supports were positioned
150 symmetrically from the midpoint of the beam, with a separation distance of 2100 mm between them.
151 These dimensions were determined based on the constraints imposed by the frame supporting the
152 radiant panel which provides the heating (see Section 2.2). Each support assembly consisted of a steel
153 roller bearing positioned between two steel plates, with one roller being securely welded to the
154 support to prevent horizontal displacement and act as a pin support. The application of loads was
155 carried out at a distance of 100 mm from the edges of the beam, i.e., 750 mm from the support
156 locations.

157 This reversed setup had several advantages. It allowed the tensioned side of the beam to be positioned
158 on the upper side, facilitating safer and more effective exposure to the radiant panel's heat flux and
159 enabling it to keep the displacements relative to the radiant panel limited without the need for
160 repositioning due to deflections.



161

162 *Figure 3. Test setup schematic overview (left); picture of the actual test set-up (right).*

163 Two 200 kN capacity hydraulic jacks with manual pressure control were used for the load application.
 164 During the test of beam B1, the pressure control was set up in a way that during the cooling phase,
 165 when the deformations started to decrease, the oil level inside the jacks did not decrease and the
 166 pressure had to be kept constant by a manual adjustment by opening the valves. This issue was resolved
 167 for the tests of beams B2 and B3, by a different configuration of the valves. In this configuration, the oil
 168 level would decrease when deformations started to decrease and the pressure was kept constant using
 169 the pump.

170 The middle 700 mm of the beams were exposed to the radiative heat flux from the panel. Considering
 171 the reversed 4-point bending setup, this is a zone with a constant bending moment (disregarding the
 172 self-weight effect). Insulation boards were used to protect the parts of the top side of the beams that
 173 should not experience heating. Furthermore, the sides of the beam were also protected with insulation
 174 boards to avoid heat losses at these zones (see Figure 4). This aimed at 1-dimensional heat transfer
 175 conditions over the height of the beam with approximately no heat losses on the sides, allowing for an
 176 adiabatic surface simplification for modelling purposes. This is confirmed by comparing the
 177 temperature results with the numerical simulations as discussed in Section 4.1.

178 Finally, in the third stage, where the residual capacity was determined, a classical 4-point bending
 179 approach was employed. The supports were positioned 100 mm from the edges of the beams, making
 180 the total span 3600 mm long. The load was applied with the loading rate of 200 N/s using the same

181 jacks as in the previous stage but now positioned 1200 mm away from the supports, making the
182 constant moment zone 1200 mm long. As the classical 4-point bending was used, the beam was
183 positioned in a way that the tensioned side of the beam (the one with 3 bars) was on the bottom.. The
184 load was increased until failure. For all beams bending failure was observed, as identified by an
185 accelerating increase in deflection at constant load. For all beams, the deflection at failure was
186 observed to be 4-5 times the deflection at the start of yielding.



187

188 *Figure 4. Insulation protection on the beams.*

189 2.4. Instrumentation

190 The load during the tests was applied with two hydraulic jacks with a capacity of 200 kN each. The load
191 was distributed to the concrete beam surface through a steel plate with dimensions of 200 mm x 200
192 mm x 40 mm. The applied forces were measured by means of two load cells with a capacity of 500 kN,
193 which were placed between the jack and the steel plate.

194 The vertical displacement was measured using the LVDTs positioned underneath both load application
195 points and at the beam midspan (the side of the beam that was not exposed to the radiant panel).
196 Furthermore, during the heating stage, Digital Image Correlation (DIC) was used to measure
197 displacements in the middle zone of the beams. No significant difference was observed between the

198 DIC and LVDT measurements of the deflections. A maximum difference of 4 % was observed. Due to
199 the insulation boards on the side of the beam and the high light intensity of the radiant panel itself,
200 only the bottom half of the beam (compressed side) was measured using DIC (see Figure 5). The DIC
201 system employs a pair of Prosilica GT3400 digital cameras, offering a combined resolution of 9
202 megapixels at 2704x3384@13 Hz on a 1-inch chip. To allow for DIC measurements, the surface of the
203 concrete beam was painted white with black speckles, as shown in Figure 5. The painted speckles have
204 sizes mainly within the range of 0.34 to 0.56 mm, while individual pixels in the images measure
205 approximately 0.10 to 0.13 mm in size. During each test, the image acquisition rate was configured to
206 operate at 1 Hz during the loading phase and 1/15 Hz during the heating and cooling phases.
207 Subsequent image processing was conducted using the VIC-3D software developed by Correlated
208 Solutions [10]. Regarding the quality of displacement measurements estimated through the DIC
209 equipment, the observed noise levels differed for in-plane and out-of-plane displacements. For in-
210 plane displacements, the noise level was quantified as approximately 0.004 mm, determined as the
211 average between the highest and lowest displacement values. Meanwhile, for out-of-plane
212 displacements, the noise level was estimated to be approximately 0.007 mm.

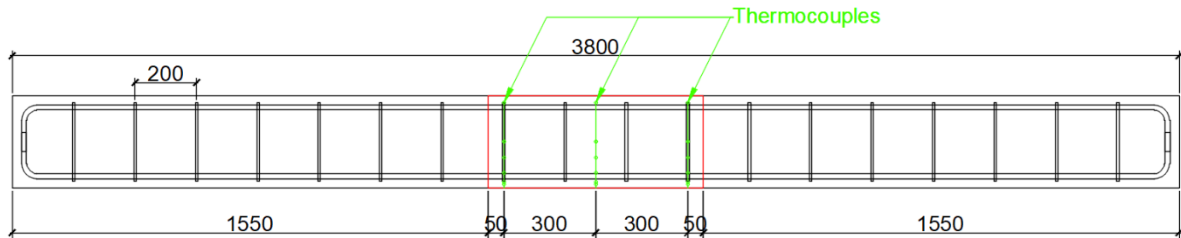


213

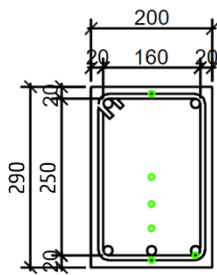
214 *Figure 5. The compressed side of the beams monitored using the Digital Image Correlation (DIC).*

215 In order to monitor the temperature distribution inside the beam, 18 type-K thermocouples (diameter
216 0.4 mm) were cast inside each beam. The thermocouples were positioned in three different positions
217 along the length of the beams: the middle sections and two sections 300 mm on each side from the
218 midpoint (refer to Figure 6). At each of these three positions, 6 thermocouples were positioned at

219 different depths from the heat-exposed surface: 12 mm (in the middle of the shear reinforcement on
 220 the outer side), 20 mm (connection of the main and shear reinforcement in the tension zone), 50 mm,
 221 100 mm, 150 mm and 278 mm (Figure 7). Their position was secured using 2 mm thick steel wire
 222 connected to the reinforcement cage of the beam, fixing the thermocouples during the casting process.



223
 224 *Figure 6. Position of the thermocouples cast inside the beams in the longitudinal direction. (red box represents the heated*
 225 *area)*



226
 227 *Figure 7. Position of the in-depth thermocouples cast inside the beams in the cross-section.*

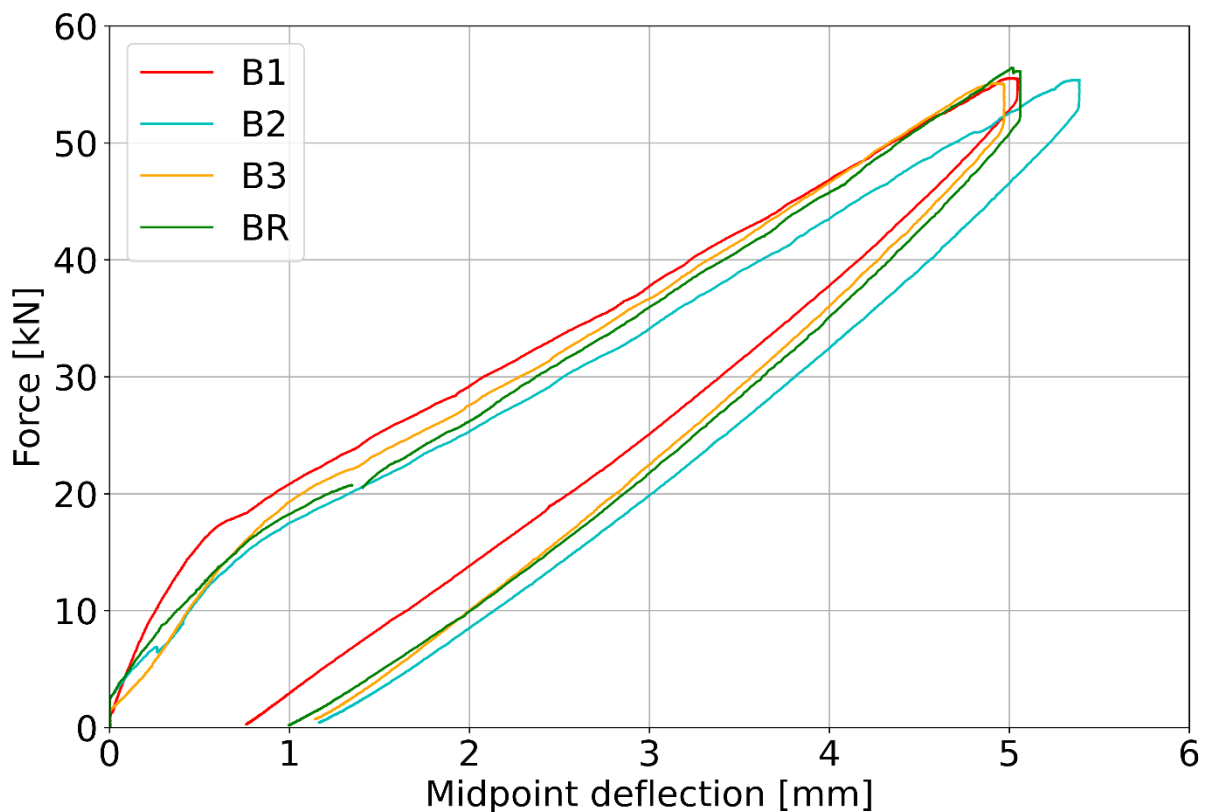
228 3. Experimental results

229 3.1. Loading and unloading phase

230 The first stage of the testing procedure, which was conducted on all beams (B1, B2, B3 and BR),
 231 consisted of the loading and unloading of the beams. This stage was conducted for the needs of the
 232 larger testing campaign, more precisely to obtain reference measurements on the beams that already
 233 experienced damage due to the expected serviceability load, but without heating exposure.

234 The beams were loaded with a loading rate of approximately 200 N/s up to a load of 55 kN on each
235 side. At this load value, the bending moment reaches a value of 41.25 kNm in the central zone of the
236 beam. This amounts to 67% of the design moment capacity of the beam.

237 Figure 8 shows the force-deflection diagram for all four tested beams. It can be noted that, as expected,
238 the behaviour of all beams is similar. The slope of the curves changes at approximately 13 kNm (17.3
239 kN force) for all beams. This is in line with the expected cracking moment of 12.7 kNm (17 kN). After
240 the unloading, the formation of the cracks in the tension zone was noticed. The cracks were on average
241 approximately 150 mm deep occurring approximately every 100 mm in the midspan zone with the
242 constant moment.



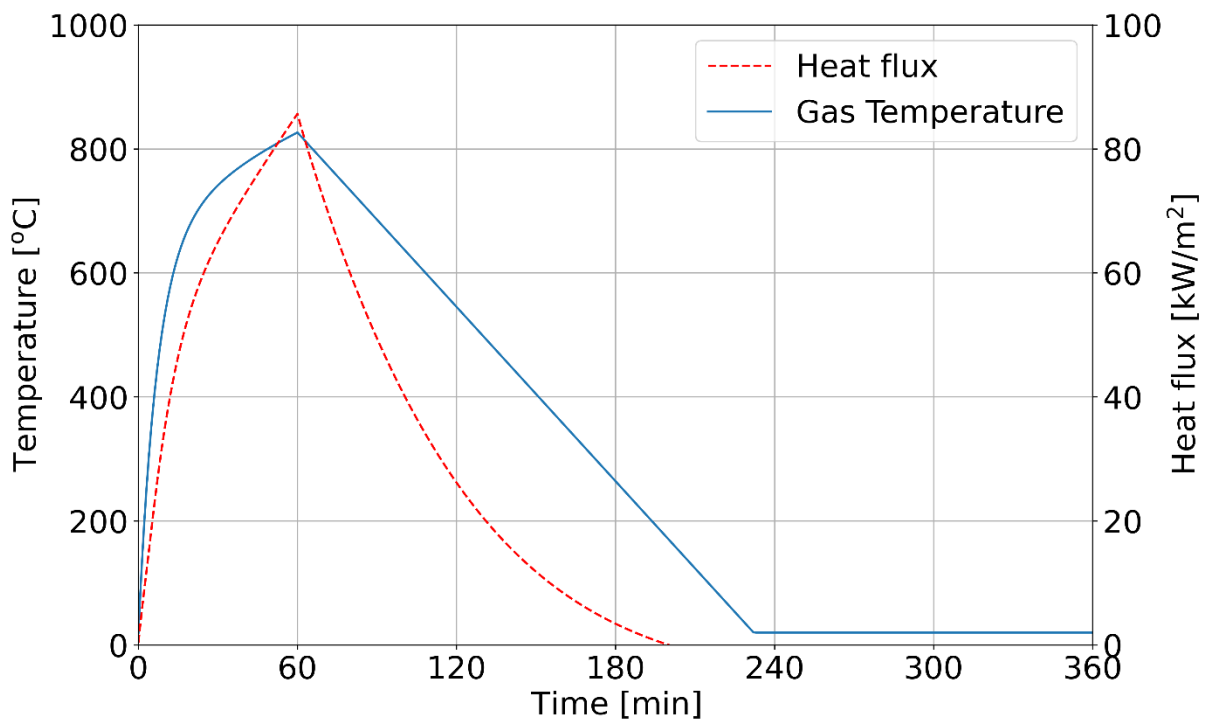
243

244 *Figure 8 Force-displacement diagram during the cracking phase of testing*

245 3.2. Fire exposure phase

246 In the fire exposure phase, natural fire exposure was simulated using the Eurocode Parametric Fire
247 Curve (EPFC) . In accordance with the capabilities of the radiant panel, EPFC with $\Gamma = 0.45$ (factor

248 defining the temperature increase during the heating phase) and a heating phase duration of 1 hour
 249 was chosen. The maximum gas temperature for this temperature-time curve is 826 °C and the total fire
 250 exposure lasts 233 min. The heat flux applied with the radiant panel is calculated in order to provide
 251 the same total heat flux to the surface of the beam as the EPFC. The radiative heat flux peaks at
 252 85.75 kW/m^2 and is stopped at 196 min when the total heat flux becomes negative (the surface
 253 temperature is higher than the gas temperature). The desired temperature-time curve and heat flux
 254 are shown in Figure 9. The beams B1, B2 and B3 were exposed to the heating 125, 140 and 182 days
 255 after casting respectively.

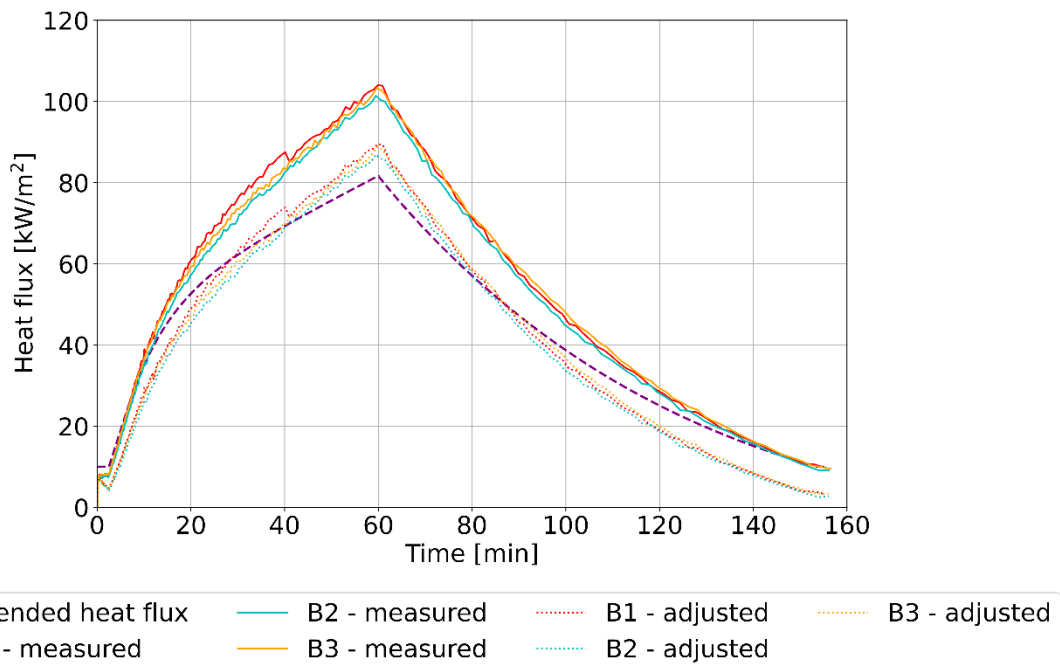


256

257 *Figure 9 Eurocode Parametric Fire Curve temperature-time curve and equivalent radiant heat flux from the panel.*

258 During the test, the heat flux at the surface of the beam was measured with a water-cooled Schmidt-
 259 Boelter heat flux meter. The heat flux meter was positioned next to the beam, levelled with the exposed
 260 surface of the beam in the middle of the exposed zone. The heat flux meter was connected to the beam
 261 in a way to stay in level with it even when the beam starts deforming. Figure 10 presents the results of
 262 the measurements for all three beams. It can be noted that the measured heat flux for all three tests
 263 was almost identical, demonstrating that all beams were exposed to the same heat flux. However, it is

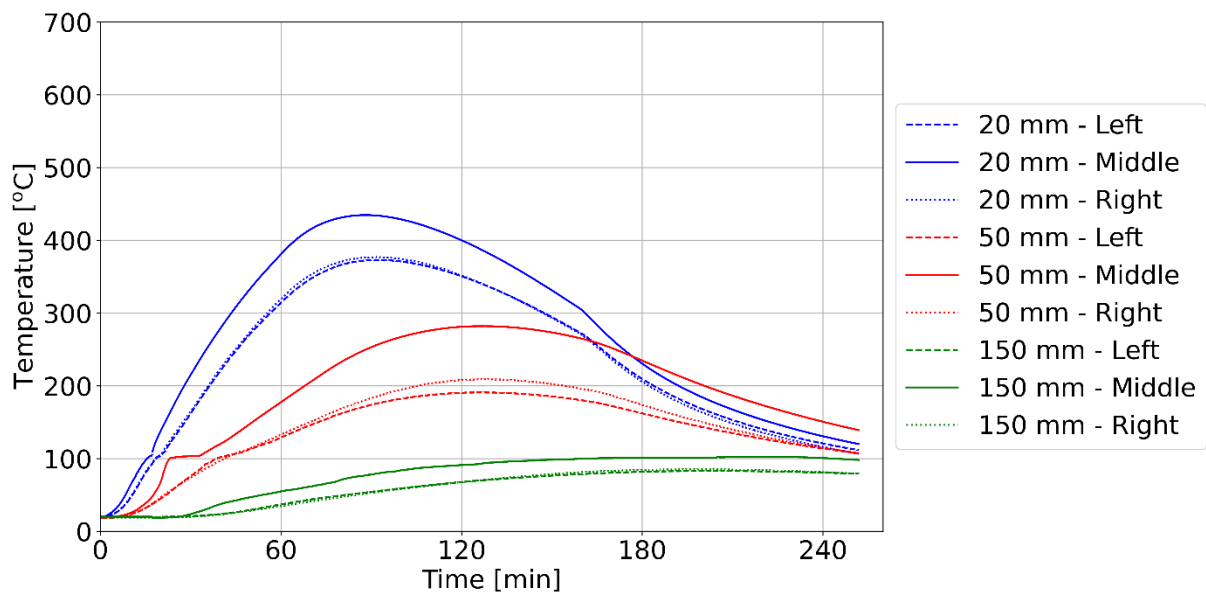
264 also clear that the measured heat flux was higher than the intended one. This difference can be mostly
 265 attributed to the effect of convection from the hot air around the heat flux meter. This convective effect
 266 was quantified, assuming that the hot air temperature around the heat flux meter is equal to the
 267 intended surface temperature of concrete using an approximate convective heat transfer coefficient of
 268 20 W/(m²K). The comparison between the measured and this adjusted heat flux suggests that the
 269 exposed surface of the beam did receive the intended radiative heat flux.



270
 271 *Figure 10 Measured and intended radiative heat flux during the tests. After 155 min, the panel was shut down and the beam*
 272 *was allowed to cool naturally.*

273 As mentioned in Section 2.4 the temperatures inside the beams were measured at 3 longitudinal
 274 positions along the beam length, using 6 thermocouples cast inside the beam at each location, as
 275 illustrated in Figure 6 and Figure 7. Figure 11 shows the measured temperature at depths of 20 mm, 50
 276 mm and 150 mm from the exposed surface for each of the three measurement locations for beam B2.
 277 Figure 10 demonstrates that the heating was symmetrical as the temperatures at the left and right
 278 sides of the heated zone are almost identical. However, the temperatures in the middle are higher. This
 279 is a consequence of the non-uniformity of the radiative heat flux (Figure 2) and the higher influence of

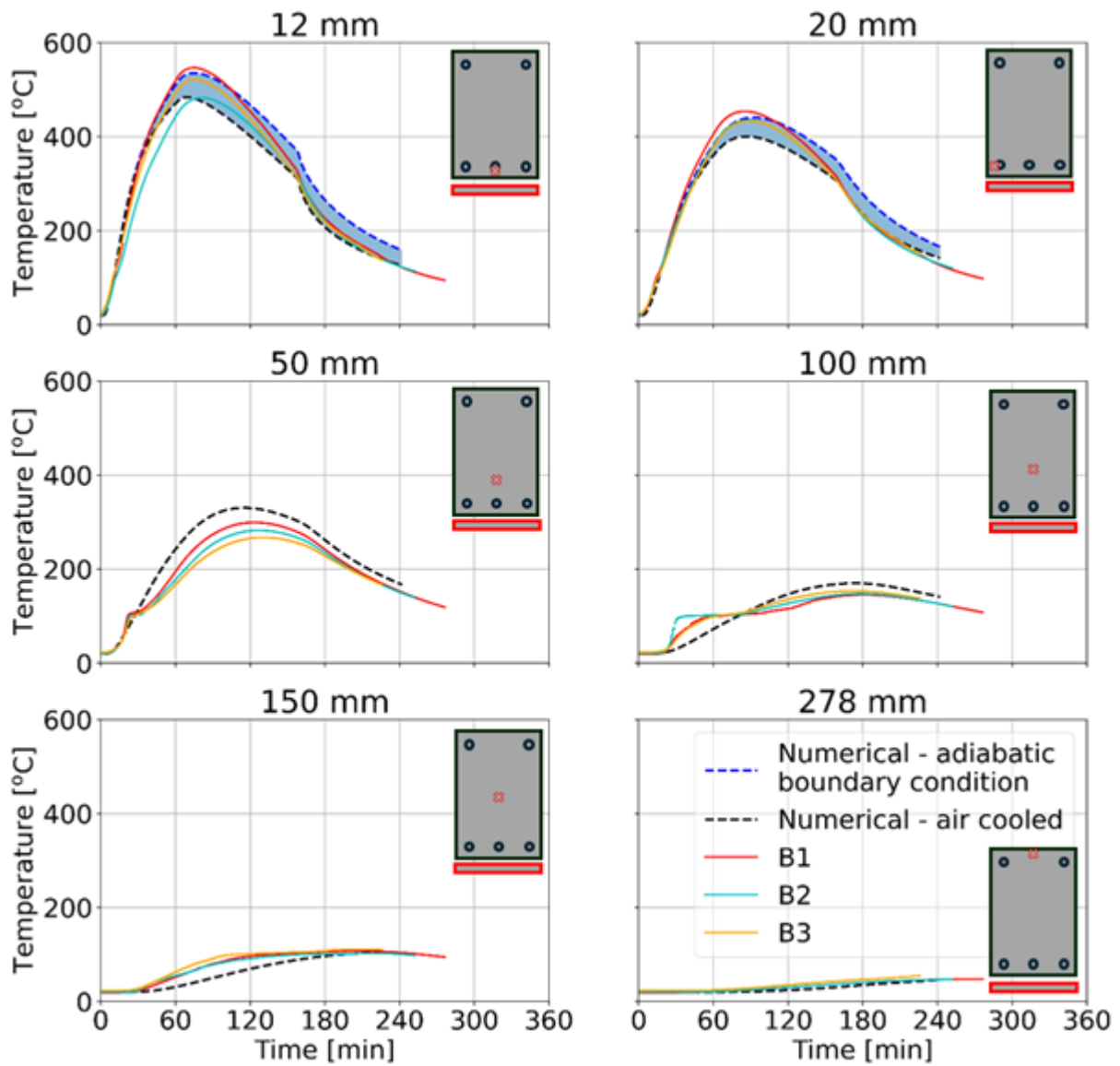
280 the heat conduction to the unheated parts of the beam. Similar results are observed in all beams and
281 at all thermocouple depths.



282

283 *Figure 11 Measured temperatures at different depths and positions during the test of beam B2.*

284 Figure 12 presents the temperatures in the middle section of all three beams at different depths. It can
285 be observed that the temperatures for all three beams do not differ significantly from each other. The
286 largest differences are closest to the exposed surface at a depth of 12 mm. The thermal gradient at this
287 position is the steepest and small variations of the thermocouple position can have a significant effect
288 on the measured temperature. However, even at this position, the temperature difference does not
289 exceed 10%. In the case of the other depths, the difference is almost negligible.



290

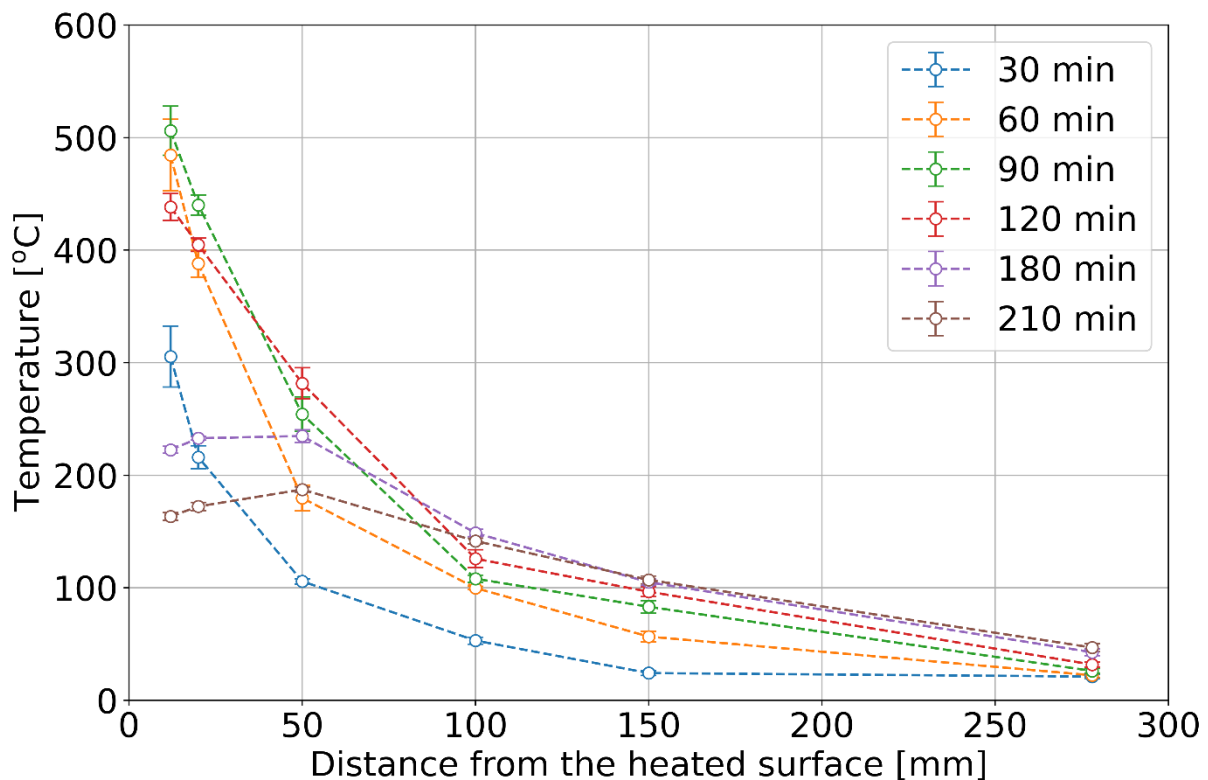
291 *Figure 12. Temperatures at the midspan section measured during all three tests at different depths compared to the numerical*
 292 *results. A distinction is made between (i) adiabatic and (ii) air-cooled numerical results related to the modelling of the*
 293 *boundary condition for the side of the beam.*

294 For all depths, especially the larger ones, a plateau at 100 °C is evident. This plateau is reached because
 295 of the moisture present inside the beam [11] and is caused by water evaporation and moisture transfer
 296 inside the beam. Additionally, it should be noted that after approximately 30 minutes in each test,
 297 water droplets on the unexposed sides of the beams were observed.

298 After, 155 minutes, when the radiative heat flux was lower than 10% of the maximum one, the panel
 299 was shut down. This moment can also be observed in Figure 12. At that point, the thermal boundary

300 condition changes, as there is no more radiative heat flux at the surface and the convective cooling
301 commences. When looking at the temperatures close to the surface (at depths of 12 and 20 mm) it is
302 evident that the cooling regime changes. At higher depths this effect is negligible.

303 In Figure 13 the temperatures in the middle of the beams at different points in time are presented,
304 considering linear interpolation between the measured temperatures at different depths in order to
305 visualize the temperature gradient. It is evident that the variation of the thermal gradient inside of the
306 beam between the tests is quite small, demonstrating again a high level of repeatability between the
307 tests. The figure also shows that even after the heating phase ends (60 min) the temperature still
308 increases deeper into the beam, as expected.

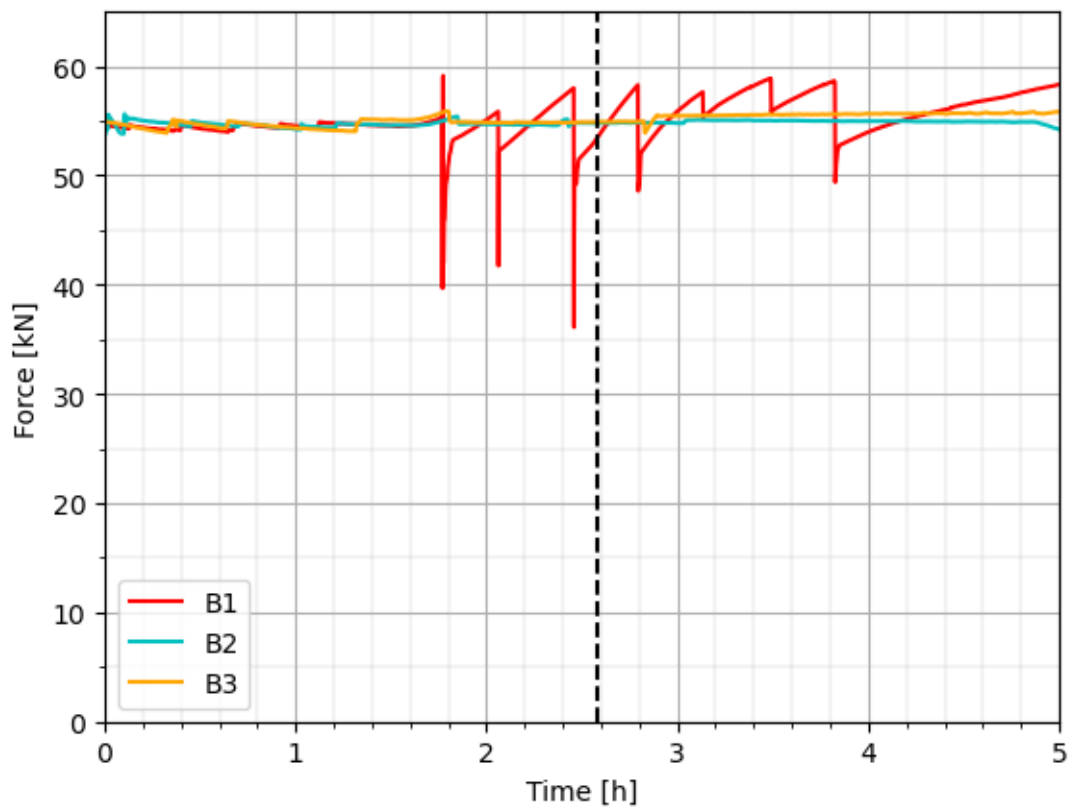


309
310 *Figure 13. Thermal gradient inside of the beams at different points in time (error bar represents the standard deviation*
311 *between the beams).*

312 The midspan deflection for all three tested beams is presented in Figure 15. The deflections are
313 presented in the form of deflection relative to the deflection at the start of the heating regime (i.e., 0
314 mm refers to the deflection under the application of the serviceability load prior to the heating regime).

315 During the first 60 minutes, while the applied heat flux was increasing, an almost linear increase in the
316 deflections can be observed. The deflections continue to increase at a slower rate until approximately
317 95 minutes when they reach their maximum for all three beams. From that point, the deflections
318 remain approximately constant for 15 min before slowly reducing. Similar to the temperatures, when
319 the panel is turned off at 155 min the rate of the decrease of deflections changes.

320 For beam B1, as mentioned in Section 2.4, the hydraulic jacks had to be controlled through a manual
321 release of pressure during the cooling phase, more precisely when deformation started to decrease.
322 This could be done only through abrupt actions and is the reason for the step-wise behaviour of the
323 deflections in Figure 13. For beams B2 and B3, this was resolved by a change in the setup of the pressure
324 control mechanism. The forces applied to the beams are presented in Figure 14.



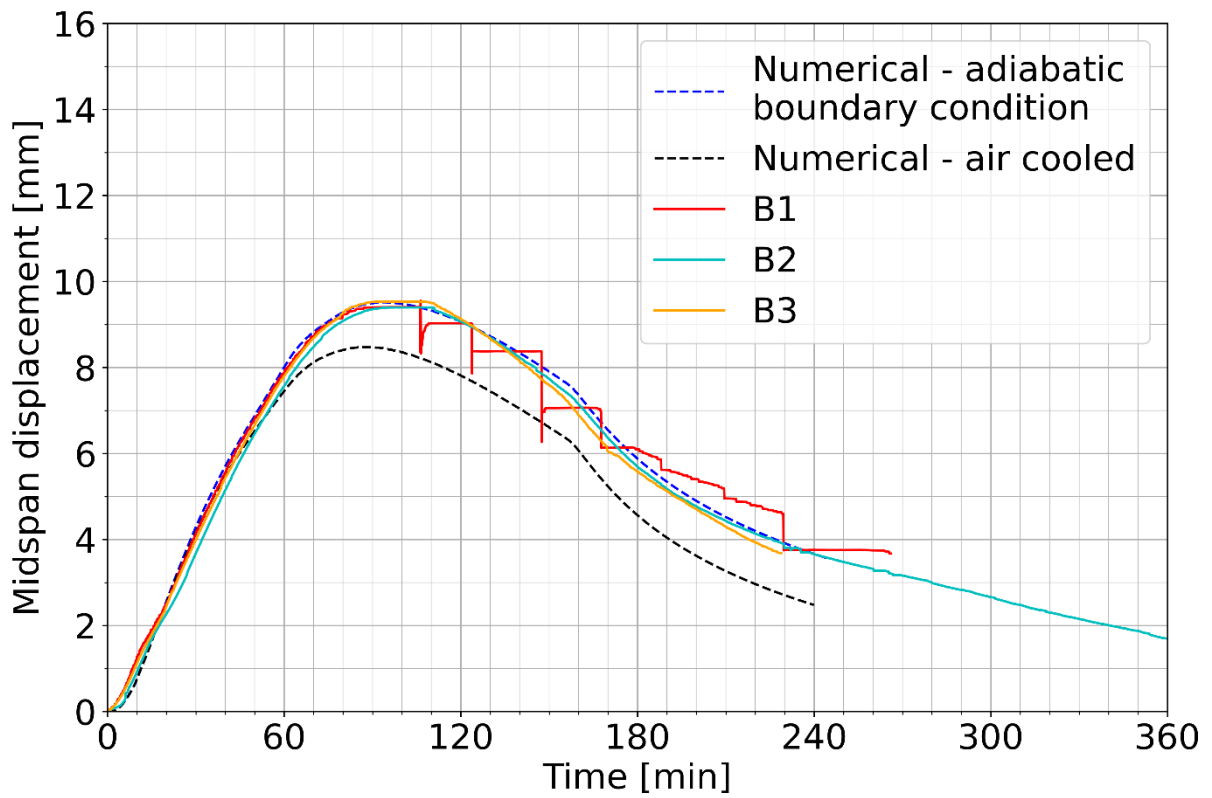
325

326 *Figure 14. Applied forces during the tests. The dashed line represents the moment when the radiant panel was shut down.*

327 The average displacements under the load application points are shown in Figure 16. The deflections
328 are presented in the form of deflection relative to the deflection at the start of the heating regime (i.e.,

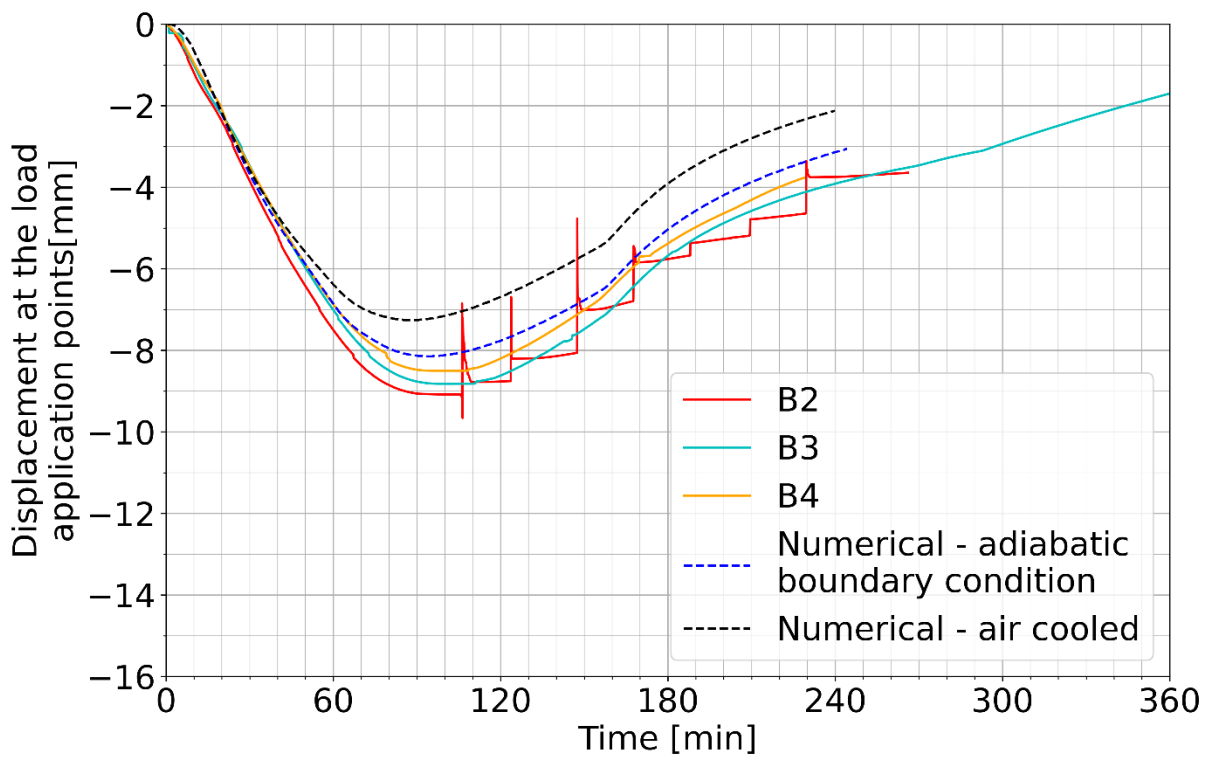
329 0 mm refers to the deflection under the application of the serviceability load prior to the heating
330 regime). Similar to the midspan deflection, the deformations under the loading points are consistent
331 between the three tested beams. Furthermore, the same general behaviour can be observed.

332 Finally, using the DIC, the curvature in the zone with the uniform moment was obtained. As the DIC
333 measurements enabled to monitor the movement for every point in this zone for the compressed half
334 of the beam, the curvature could be calculated using two different approaches. Firstly, the average
335 vertical displacement was calculated for every 1 cm wide vertical strip of the monitored area. These
336 deformations show an almost perfect match to the parabolic curve. The curvature was obtained as the
337 second derivative of this curve. The second approach consisted of obtaining the total strain diagram in
338 the function of the height, averaged out on the whole monitored area. These total strain diagrams
339 showed a linear trend, validating the assumption in the Euler-Bernoulli beam theory of plain sections
340 remaining plain, even at elevated temperatures. The curvature is calculated as the slope of this total
341 strain diagram. These two methods produced almost identical results with less than 2% difference in
342 the values. The change of the curvature in the heated zone is shown in Figure 17 (using the first
343 method) and similar trends as for the midspan and load point deformations can be observed.



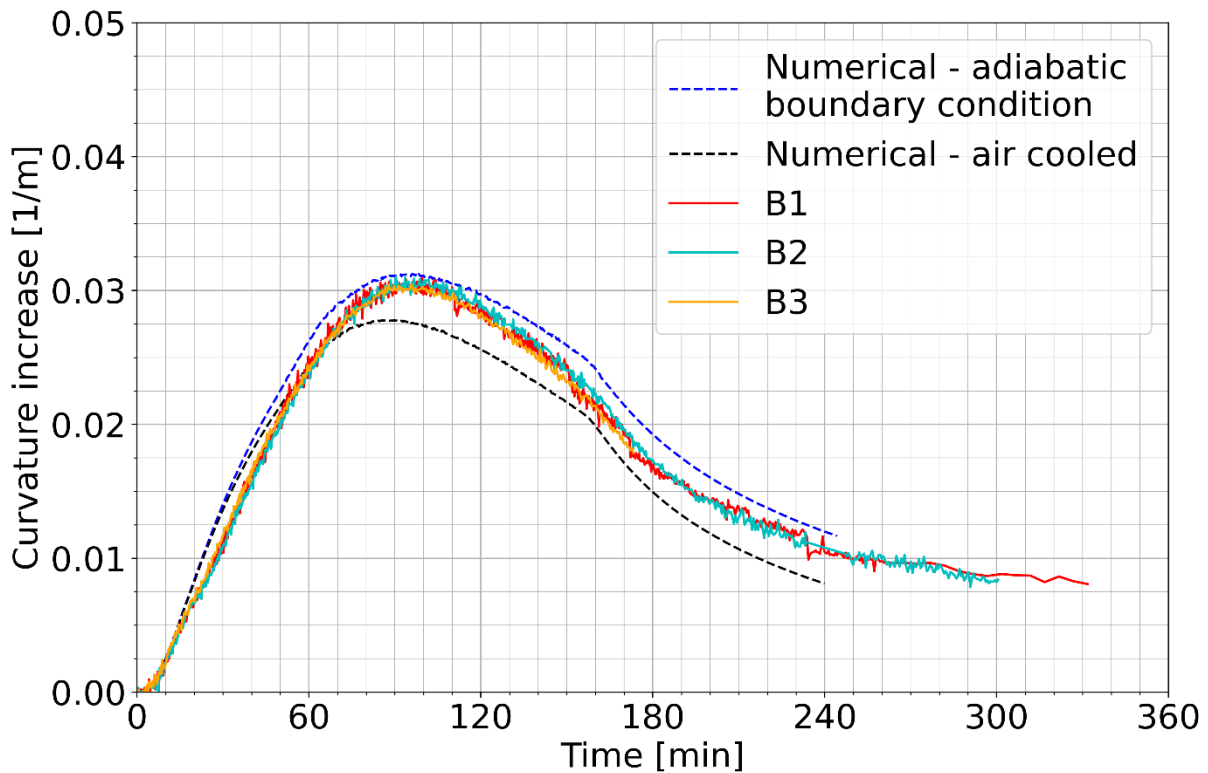
344

345 *Figure 15. Midspan displacement during the tests compared to the results of numerical simulations*



346

347 *Figure 16 The average displacement at the load application points during the tests compared to the results of numerical*
 348 *simulations.*



349

350 *Figure 17. Curvature increase during the tests compared to the results of numerical simulations.*

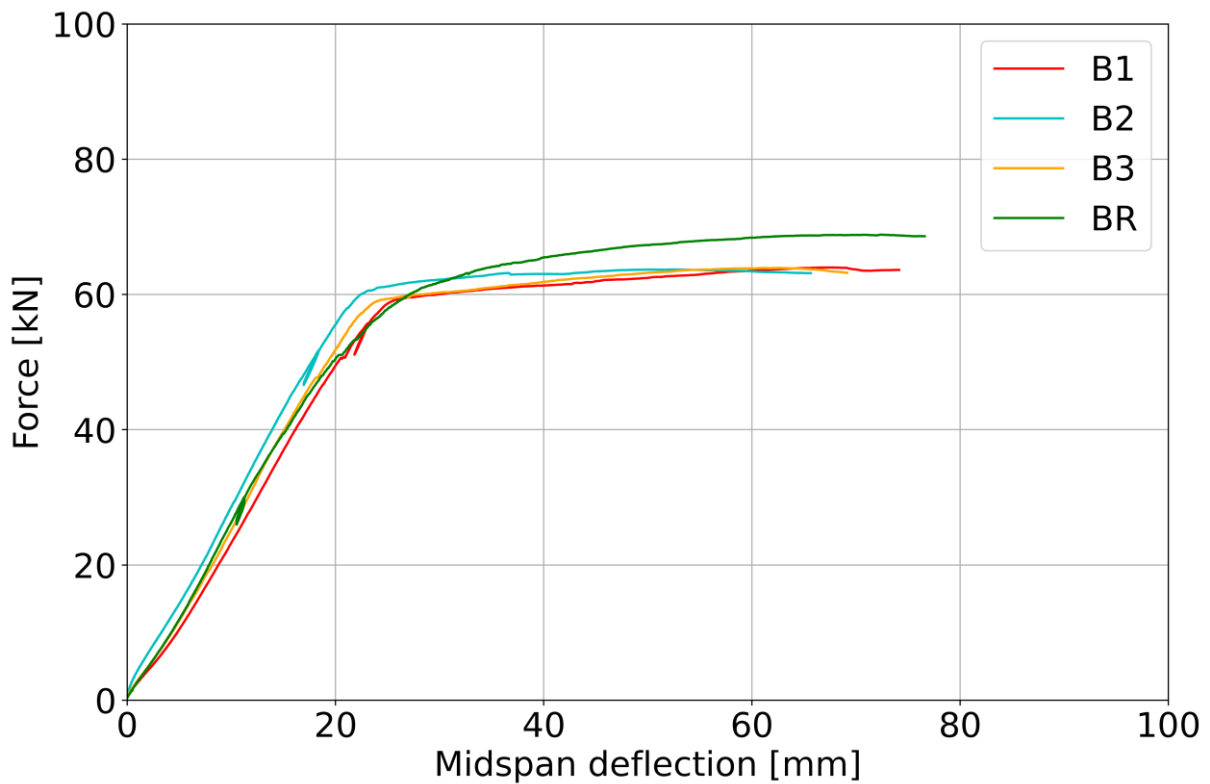
351 3.3. Residual capacity tests

352 This stage was conducted on both the beams exposed to elevated temperature (B1-B3) and the
 353 reference beam BR. Its purpose was to determine the residual bending capacity of beams B1-B3 and
 354 compare it to the residual bending capacity of the non-fire exposed beam BR. For that purpose, a
 355 standard 4-point bending setup was employed. These tests were conducted 160, 147 and 107 days
 356 after the heat exposure for the beams B1, B2 and B3 respectively. Figure 18 shows the force–midspan
 357 deflection diagram for all the beams. From the figure, it is evident that the heating exposure did not
 358 have a large effect on the bending stiffness of the beams, as the initial slope of the curve for the beam
 359 BR is similar to the slope of heat-exposed beams. However, the overall shape of the curves differs. For
 360 beams B1-B3 a linear behaviour is observable until a deflection of about 25 mm is reached, which is
 361 the onset of a clear plateau in the diagram.

362 In the case of the bending moment capacity, there appears to be a significant difference between them.

363 The values of the bending moment capacity are shown in Table 2. The coefficient of variation of the

364 values for beams B1-B3 is 0.2%, while the value for BR is around 8% higher demonstrating a clear
 365 reduction in the ultimate bending capacity due to the heat exposure.



366

367 *Figure 18. The force–midpoint deflection diagram for beams B1-B3 and BR during the residual capacity tests.*

368 *Table 2. Ultimate bending moment capacity of the beams B1-B3 and BR*

Beam	B1	B2	B3	BR
Bending capacity - M_R [kNm]	76.8	76.4	76.7	82.6

369

370

371 4. Numerical modeling

372 A finite element model of the tested beams was developed in the finite element software SAFIR [12],

373 which specializes in the modelling of the structural behaviour of structures exposed to fire. The analysis

374 consists of two parts. First, the heat transfer analysis is conducted in order to obtain the temperature-
375 time history of the structure and afterwards, that data is used to conduct the structural analysis.

376 4.1. Heat transfer

377 The heat transfer analysis was conducted considering a 2-dimensional model focusing on the heat
378 transfer inside the cross-section. The cross-section was divided into 1320 rectangular elements with
379 size varying from 4 to 8 mm. The concrete was modelled as defined in EN 1992-1-2 (3.3) [7]
380 (SILCON_EN). The default values were used: concrete density $\rho_{con} = 2400 \frac{kg}{m^3}$, water content $w =$
381 $46 kg/m^3$ and thermal conductivity as average of upper and lower limit. The steel reinforcement was
382 modelled according to thermal properties defined in EN 1993-1-2 . The radiation and convection
383 boundary conditions are considered for the tensioned edge of the cross-section using a single
384 temperature-time curve. As stated in Section 3.2 (Figure 9), the temperature-time curve considered
385 was an EPFC with $\Gamma = 0.45$ and a heating phase duration of 1h. As the panel was shut down after 155
386 min, the cooling branch of the EPFC was modified as follows: the EPFC cooling branch was followed up
387 to 155 min, after which the temperature-time curve was considered to instantaneously drop to 20 °C.
388 The radiative heat transfer considered an absorptivity/emissivity of the concrete surface of 0.7 and
389 convection was calculated considering a convection coefficient of 35 W/(m²K), both in accordance with
390 the Eurocode provisions . On the compressed side, convective and radiative heat losses are considered
391 relative to a constant reference temperature of 20 °C. This was done considering an emissivity of 0.7
392 and a convection coefficient of 4 W/(m²K) .

393 As mentioned before, the sides of the beams were protected from the incoming radiation using
394 insulation boards. However, to enable additional instrumentation, an air gap of approximately 15 mm
395 between the board and the beam was left. As the air in the gap would work as an insulation, the actual
396 boundary condition on the sides was close to the perfect insulation and it was modelled in that way
397 (i.e., adiabatic boundary condition).

398 In Figure 12 the results of the heat transfer analysis are shown together with the measurements of the
399 thermocouples during the test. Overall it can be concluded that the simulation results correspond well
400 with the measured values at all depths. At larger depths, we can see that the numerical simulation is
401 not able to properly capture the plateau at 100 °C. This is a commonly known shortcoming of the heat
402 transfer calculations of concrete members where the moisture transfer is neglected, see e.g., [13]. Even
403 though the energy of evaporation is accounted for in the specific heat of concrete definition according
404 to EN 1992-1-2 [7], it assumes that moisture is uniformly distributed over the entire cross-section for
405 the full duration of the heat exposure. However, in reality, due to the thermal effects, the moisture
406 content migrates to the cooler parts. For this reason, we can observe a faster rise to 100 °C in the
407 measured data at higher depths, as more energy is brought with the moisture transfer, which
408 condenses in the cooler zones of the concrete, increasing the moisture concentration there [14].
409 Because of this increased moisture concentration, the energy needed for evaporation is higher which
410 in turn causes a longer plateau.

411 4.2. Structural analysis

412 In the structural analysis, the beam is modelled as a 2-dimensional fibre model (the determination of
413 forces and stiffness in the section is based on the temperatures in each element used in the thermal
414 analysis which form a fibre in the beam element) with a length of a 3.6 m (distance between the load
415 application points), consisting of 72 elements of 0.05 m length. For the middle 14 elements, the
416 temperature-time history as obtained through the previously discussed heat transfer calculations is
417 used, while the other elements remain at a temperature of 20 °C throughout the whole simulation.
418 The mechanical boundary conditions are modelled as they were implemented in the tests (roller and
419 pin support) and the load is introduced as two vertical forces with a constant value of 55 kN positioned
420 at the ends of the beam.

421 The concrete model used is a direct implementation of the explicit transient creep model introduced
422 by [15] (SILCON_ETC). Input material properties needed for this model were based on the measured

423 values: concrete compressive and tensile strength $f_c = 45.7 \text{ MPa}$ and $f_t = 2.9 \text{ MPa}$. During the
424 cooling process, the mechanical properties of strength and strain at peak stress are not recoverable. A
425 further reduction of 10% in the concrete's compressive strength, relative to the value at the maximum
426 temperature reached, is accounted for during cooling, as outlined in [16]. The reinforcement was
427 modelled using the model which is defined in EN 1992-1-2 (3.3) [7] (STEELEC2EN), similarly, the
428 measured yield strength of $f_y = 565 \text{ MPa}$ is used together with the modulus of elasticity $E_s =$
429 213 GPa as needed input values.

430 A comparison of the calculated midspan deformation with the ones measured during the tests is
431 presented in Figure 15. Overall, the model is able to predict the behaviour observed in the tests rather
432 accurately. This is also highlighted by the fact that the simulation results do not differ from the
433 measured values more than the three identical beams tested in a fundamentally identical way differ
434 from each other.

435 The agreement between the numerical simulation and measured results is much higher in the case
436 where the boundary condition on the side edges is modelled as adiabatic. This observation is in line
437 with the previous observation that the agreement between temperatures is also higher in this case,
438 especially in the heating phase.

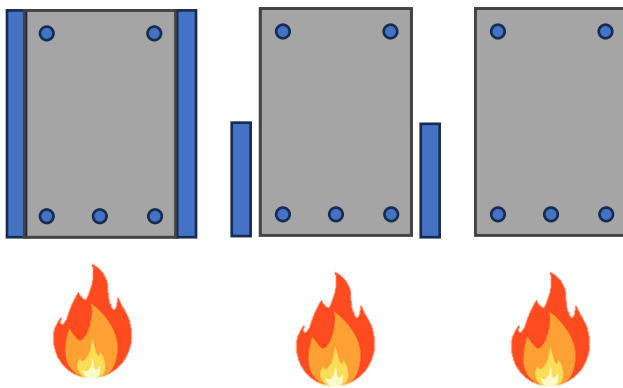
439 Similar agreements can also be seen in Figure 16 which represents the additional deflection during the
440 heating and cooling of the beam at the position of the load points (i.e., the beam extremities). When
441 the curvature behaviour is analyzed in Figure 17, a very close agreement between the tests and model
442 is obtained

443 5. Discussion

444 The heat transfer was modelled with perfect insulation. However, due to the existence of the air gap
445 during the tests, the real heat loss condition is quite difficult to model precisely. In order to assess this,
446 the boundary condition on the side edges was modelled in an additional way. It was modelled as the

447 side edges are exposed to the ambient air, by considering the same cooling conditions as for the
448 compressed edge. This is illustrated in Figure 19.

449 The test results show better agreement with the case where the side edges are modelled as adiabatic,
450 especially in the first 120 min, afterwards the shift to the case with the ambient air on the sides is
451 observed. This can be explained by the air temperature in the gap during the test. It can be assumed
452 that during the heating phase of the test, the air temperature also rose causing any heat transfer on
453 the side negligible. After the temperatures of the beam started dropping the air in the gap, due to its
454 thermal properties, started to cool down faster and caused faster cooling of the sides of the beams.
455 The effect of the different boundary conditions on the side edges is almost negligible at larger depths.



456

457 *Figure 19. Different cases for modelling boundary conditions on the side edges of the concrete beams: full insulation (left), real*
458 *scenario during the tests (middle; this case is not directly modelled) and ambient air contact (right).*

459 When considering the residual bending capacity, it can be noted that the three beams exposed to
460 elevated temperatures showed great uniformity in the obtained bending capacity with a 0.2%
461 coefficient of variation. The three beams show an 8% lower capacity than the reference beam BR. The
462 source of this difference can be traced to the reduction of the yield strength of the reinforcing steel as
463 the temperature in the compressed half of the beams B1 to B3 never reached more than 100 °C. Even
464 though it is commonly agreed that the reinforcement steel retains 100% of its yield strength after
465 cooling when its temperature does not exceed 500 °C [17], as was the case for beams B1 to B3,
466 experimental data from [18], [19], [20], [21], shows that a reduction of for this temperature range, of

467 order of magnitude of 0-7% has been recorded. Considering that, an 8% reduction in ultimate bending
468 capacity due to a decrease in reinforcement yield strength is a reasonable hypothesis, however a
469 further investigation in the future is needed to confirm this.

470 6. Conclusions

471 An innovative electric radiant panel has been used in order to simulate a natural fire exposure of
472 concrete beams. The tests described herein are conducted to produce three identically fire-damaged
473 beams, which are tested to assess their post-fire condition. Despite minor limitations related to the
474 heated area's size and the maximum heat flux, it showed great performance in the sense of control and
475 repeatability. The preliminary phase, involving mechanical loading and unloading tests, yielded crucial
476 baseline data, with the observed crack formations aligning with theoretical expectations.

477 Temperature measurements within the beams demonstrated an almost uniform thermal field between
478 all the beams, with minor discrepancies easily attributed to precise thermocouple placement.
479 Comparisons with numerical simulations of the temperature field confirmed the efficacy of the
480 experimental setup in replicating natural fire conditions, notably the EPFC temperature-time curve,
481 despite the panel producing only a radiative heat flux.

482 The structural response of the beams during the heating phase exhibited distinct phases. Initially, there
483 was a linear increase in deflection, followed by a slower rate of deflection increase. The beams reached
484 their maximum deflection, after which they exhibited a plateau before slowly reducing deflections
485 during the cooling phase. These observations align with expected behaviour under fire exposure
486 conditions. A similar high level of repeatability and consistency is observed to the one observed with
487 temperatures. Deformations for all three beams are similar to each other, showing the same trends
488 both in the heating and cooling.

489 In regards to the residual bending capacity of the beams, the results showed large uniformity across
490 the beams exposed to elevated temperature. The beam not exposed to high temperatures showed a

491 slightly higher bending capacity, effectively demonstrating that some amount of damage occurred due
492 to temperature exposure.

493 The FEM analysis proves to be a precise tool for simulating the behaviour of concrete members
494 subjected to fire conditions. Prior modelling with readily available state-of-the-art simulation tools align
495 very well with the observed test results. Thus, the test results can be considered as a validation of said
496 the applied simulation tools. Modelling using SAFIR has proven to be able to assess the temperature
497 field in the beams with reasonable accuracy. The inability to model the moisture transfer is a deficiency,
498 especially when higher depths are considered, however, they do not have a large effect on the global
499 behaviour of the member.

500 The model accurately predicted the structural response during the heat exposure. The differences
501 between the numerical results and the tests' results are on the same scale as the differences between
502 the tests themselves. A high potential for assessing concrete member behaviour in fire scenarios is
503 demonstrated based on these results.

504 In summary, this research contributes to the field of fire engineering by demonstrating a reliable and
505 innovative testing approach for simulating fire-induced damage on concrete members. The use of a
506 innovative electric radiative panel, combined with accurate natural fire exposure conditions, offers a
507 promising avenue for evaluating the post-fire behaviour of concrete structures. The repeatability and
508 consistency of results across multiple tests enhance the credibility of the findings. Furthermore, the
509 applied numerical simulations' accuracy reinforces their potential utility in assessing and predicting
510 concrete structures' behaviour under fire conditions.

511 Acknowledgements

512 The authors wish to thank the Research Foundation of Flanders (FWO) for the financial support on the
513 research project (Grant number 3G010220) "Vibration-based post-fire assessment of concrete
514 structures using Bayesian updating techniques". Andrea Lucherini is funded by the FRISSBE project

515 within the European Union’s Horizon 2020 research and innovation program (GA 952395) and Florian
516 Put is funded by Research Foundation of Flanders (FWO) within the scope of the research project (Grant
517 number 1137123N) “Characterization of the thermal exposure and material properties of concrete
518 during the fire decay phase for performance-based structural fire engineering”. The authors further
519 thank dr. Ramin Yarmohammadian for the useful comments on the manuscript.

520 References

- 521 [1] J. Beitel and N. Iwankiw, “Historical Survey of Multi-Story Building Collapses Due to Fire,” *Fire Prot.*
522 *Eng.*, vol. 27, 2005.
- 523 [2] fib, Fédération International du Béton, *fib Bulletin 108. Performance-based fire design of concrete*
524 *structures*. 2023. doi: 10.35789/fib.BULL.0108.
- 525 [3] B. Jovanović, R. Caspeepele, G. Lombaert, E. Reynders, and R. Van Coile, “State-of-the-art review on
526 the post-fire assessment of concrete,” *Struct. Concr.*, 2023.
- 527 [4] fib Fédération International du Béton, *Fib bulletin 38: fire design of concrete structures—materials,*
528 *structures and modelling, state-of-the art report*, vol. 53. 2007.
- 529 [5] T. Gernay *et al.*, “Experimental investigation of structural failure during the cooling phase of a fire:
530 Concrete columns,” *Fire Saf. J.*, vol. 134, p. 103691, Dec. 2022, doi: 10.1016/j.firesaf.2022.103691.
- 531 [6] C. Maluk, L. Bisby, M. Krajcovic, and J. L. Torero, “A Heat-Transfer Rate Inducing System (H-TRIS)
532 Test Method,” *Fire Saf. J.*, vol. 105, pp. 307–319, Apr. 2019, doi: 10.1016/j.firesaf.2016.05.001.
- 533 [7] CEN, “EN 1992-1-2:2004: Eurocode 2: Design of concrete structures - Part 1-2: General rules.
534 Structural fire design.” European Standard, 2004.
- 535 [8] F. Put, B. Jovanović, E. Symoens, A. Lucherini, B. Merci, and R. Van Coile, “High-Intensity Fast-
536 Response Electric radiant Panel (HIFREP) for increased accuracy on thermal boundary conditions
537 during fire testing,” *4th Eur. Symp. Fire Saf. Sci. – ESFSS 2024*, in press.
- 538 [9] A. Lucherini and J. L. Torero, “Defining the fire decay and the cooling phase of post-flashover
539 compartment fires,” *Fire Saf. J.*, vol. 141, p. 103965, Dec. 2023, doi: 10.1016/j.firesaf.2023.103965.

- 540 [10] Correlated Solutions, *Vic-3D*. (2010). Correlated Solutions Inc. [Online]. Available:
541 www.correlatedsolutions.com/supportcontent/VIC-3D-8-Manual.pdf
- 542 [11] H. Lakhani, P. Kamath, P. Bhargava, U. Sharma, and G. Reddy, "Thermal Analysis of Reinforced
543 Concrete Structural Elements," *J. Struct. Fire Eng.*, vol. 4, no. 4, pp. 227–244, Jan. 2013, doi:
544 10.1260/2040-2317.4.4.227.
- 545 [12] J.-M. Franssen and T. Gernay, "Modeling structures in fire with SAFIR®: theoretical background
546 and capabilities," *J. Struct. Fire Eng.*, vol. 8, no. 3, pp. 300–323, Jan. 2017, doi: 10.1108/JSFE-07-
547 2016-0010.
- 548 [13] J. V. Aguado, V. Albero, A. Espinos, A. Hospitaler, and M. L. Romero, "A 3D finite element model
549 for predicting the fire behavior of hollow-core slabs," *Eng. Struct.*, vol. 108, pp. 12–27, 2016.
- 550 [14] T. Z. Harmathy, "Effect of Moisture on the Fire Endurance of Building Elements," in *Moisture in*
551 *Materials in Relation to Fire Tests*, A. F. Robertson, Ed., 100 Barr Harbor Drive, PO Box C700, West
552 Conshohocken, PA 19428-2959: ASTM International, 1965, pp. 74-74–22. doi:
553 10.1520/STP48429S.
- 554 [15] T. Gernay and J. M. Franssen, "A formulation of the Eurocode 2 concrete model at elevated
555 temperature that includes an explicit term for transient creep," *Fire Saf. J.*, vol. 51, pp. 1–9, 2012,
556 doi: 10.1016/j.firesaf.2012.02.001.
- 557 [16] CEN, "EN 1994-1-2:2005 Eurocode 4: Design of composite steel and concrete structures - Part 1-2
558 General rules - Structural fire design," *European Standard*. European Standard, 2005.
- 559 [17] V. K. R. Kodur and A. Agrawal, "An approach for evaluating residual capacity of reinforced concrete
560 beams exposed to fire," *Eng. Struct.*, vol. 110, pp. 293–306, 2016, doi:
561 10.1016/j.engstruct.2015.11.047.
- 562 [18] I. C. Neves, J. P. C. Rodrigues, and A. de P. Loureiro, "Mechanical Properties of Reinforcing and
563 Prestressing Steels after Heating," *J. Mater. Civ. Eng.*, vol. 8, no. 4, 1996, doi: 10.1061/(asce)0899-
564 1561(1996)8:4(189).

- 565 [19] J. Outinen and P. Mäkeläinen, "Mechanical properties of structural steel at elevated temperatures
566 and after cooling down," *Fire Mater.*, vol. 28, no. 2–4, pp. 237–251, 2004, doi: 10.1002/fam.849.
- 567 [20] A. Y. Elghazouli, K. A. Cashell, and B. A. Izzuddin, "Experimental evaluation of the mechanical
568 properties of steel reinforcement at elevated temperature," *Fire Saf. J.*, vol. 44, no. 6, pp. 909–
569 919, Aug. 2009, doi: 10.1016/j.firesaf.2009.05.004.
- 570 [21] R. Felicetti, P. G. Gambarova, and A. Meda, "Residual behavior of steel rebars and R/C sections
571 after a fire," *Constr. Build. Mater.*, vol. 23, no. 12, pp. 3546–3555, Dec. 2009, doi:
572 10.1016/j.conbuildmat.2009.06.050.
- 573